

Load-level isolator model for pallets on industrial storage racks and validation with experimental results

Marcelo Sanhueza-Cartes¹, Nelson Maureira-Carsalade^{*1}, Eduardo Núñez¹ and Ángel Roco-Videla²

¹Facultad de Ingeniería, Universidad Católica de la Santísima Concepción, Concepción, Chile

²Universidad Arturo Prat, Iquique-Chile

(Received August 29, 2023, Revised June 18, 2024, Accepted June 20, 2024)

Abstract. This paper introduces a system allows for seismic isolation of the pallet from the rack in the down-aisle direction, occupies minimal vertical space (5 cm) and ± 7.5 cm of deformation range. A conceptual model of the isolation system is presented, leading to a constitutive equation governing its behavior. A first experimental campaign studying the response of the isolation system's components was conducted to calibrate the parameters of its constitutive equation. A second experimental campaign evaluated the response of the isolation system with mass placed on it, subjected to cyclic loading. The results of this second campaign were compared with the numerical predictions using the pre-calibrated constitutive equation, allowing a double-blind validation of the constitutive equation of the isolation system. Finally, a numerical evaluation of the isolation system subjected to a synthetic earthquake of one component. This evaluation allowed verifying attributes of the proposed isolation system, such as its self-centering capacity and its effectiveness in reducing the absolute acceleration of the isolated mass and the shear load transmitted to the supporting beams of the rack.

Keywords: constitutive numerical model; double-blind validation; down-aisle direction; experimental tests; pallet isolation

1. Introduction

Industrial storage racks are among the most vulnerable structures system against seismic action (Beattie, 2006). This has been evident during recent earthquakes, such as the Darfield earthquake that occurred in September 2010 in the city of Christchurch (Crosier *et al.* 2010). During an inspection conducted by a group of researchers from the USA and New Zealand in various industrial buildings, damages that varied from moderate to total collapse were identified in industrial storage racks. These results are consistent with the findings of Uma and Beattie (2011) and Clifton *et al.* (2011), who reported observing severe damage to this type of structure as well as storage losses. On the other hand, Perrone *et al.* (2019) conducted a study on the seismic behavior of non-structural elements during the 2016 Central Italy earthquake. They observed severe damage to industrial storage racks, primarily due to overturning and buckling of the columns. According to Miranda *et al.* (2012), during the 2010 Maule-Chile earthquake, considerable damage was also identified in Chilean industrial storage racks. Rossi *et al.* (2019) mention that the inadequate seismic performance of this type of structures is mainly due to the lack of detailing in its general design and connections to support lateral forces.

Currently, industrial storage racks are growingly in demand due to the rise in e-commerce and the growth of the

logistics sector (Donà *et al.* 2022). These structures are increasingly used in commercial spaces and open to the public, so a structural failure and even the fall of pallets represents a potential danger for clients and workers (Alhan and Gavin 2005, FEMA 460 2005, Sideris *et al.* 2010). Due to the different problems that racks have faced during seismic events, different effects have been produced in the industry, such as: monetary losses, human losses and indirect losses due to business interruption (Brown *et al.* 2015, Donà *et al.* 2019). Some authors have proposed mitigation solutions to reduce lateral accelerations in industrial storage racks due to seismic loading, in addition to proposals to improve their performance and safety in general (Donà *et al.* 2022). These mitigation solutions are mainly based on passive type seismic protection systems, such as energy dissipation, tuned mass dampers and seismic isolation. When implementing any of these technologies, there is also an increase in the cost of the rack. Regarding this, Kilar *et al.* (2013), evaluated the economic feasibility of implementing seismic isolation to an industrial storage rack. They obtained that for ground motion intensities ranging from low to moderate, when only a repair of the structure is required, the retrofit using such technology is not economically viable. While, for higher intensities of earthquakes, when there is an interruption of the business activity due to rack damage, falling merchandise or collapse of the rack in general, the implementation of this type of technology could be of great benefit.

Among the specific energy dissipation devices to protect industrial storage racks is the base plate - column connection proposed by Tang *et al.* (2017). This proposal consists of the insertion of a steel sliding friction plate

*Corresponding author, Ph.D.
E-mail: nmaureira@ucsc.cl

placed at each base joint of the columns, which is designed for low and medium height racks. The clamping force is related to the tightening of the bolts and the energy dissipation capacity can be adapted to the design needs. These authors mention that the proposed friction base plate can achieve up to 20% equivalent damping. Following the significant loss of “Parmigiano Reggiano” cheese due to the 2012 Emilia-Romagna earthquake in Italy (Mucciarelli and Liberatore 2014), Franco *et al.* (2015) proposed using viscous dampers to connect the tops of the storage racks to the surrounding concrete structure. Maureira-Carsalade *et al.* (2023), propose an energy dissipation device for tension loads with self-centering capacity that can also be used to protect industrial storage racks. They mention that, since the device can only work under tension loads, to be used in racks it should be implemented in pairs of post-tensioning loaded crossed diagonal in a bracing tower. As a last example, Shaheen and Rasmussen (2022), propose a friction-damped seismic fuse for use in industrial storage rack bracing. This device is made up of five parts: a brace, a seismic fuse, a steel tube, bolts and nuts. In this solution, the contact pressure between the parts can be regulated by tightening the bolts, temporarily blocking the braces and thus preventing slipping for small lateral loads. After the lateral force overcomes the frictional force supplied by the pressure of the bolts, the fuse begins to oscillate in tension and compression, allowing the rack to become more flexible. This device demonstrated that its implementation could generate a significant reduction in the base shear load and improve the overall seismic performance of the rack. Additionally, equivalent damping of up to 15% can be achieved.

The first seismic isolation device developed specifically for racks was invented and studied by Gutelius *et al.* (2000), and its focus was the protection of sensitive electronic equipment such as computers and servers. Subsequently, device of isolation seismic specifically to protect industrial storage racks was developed (Pellegrino *et al.* 2007, Filiatrault *et al.* 2008, Michael *et al.* 2010). This device could isolate the structure from ground motion only in the cross-aisle direction, with scarce effect in the down-aisle direction. Other devices of seismic isolation developed more recently are described in the review of the literature conducted by Simoncelli *et al.* (2020). One of the devices described by these authors corresponds to the isolation of LOKIBASE base (Ferrari 2019), which can isolate the structure in any horizontal direction, with the disadvantage that it cannot withstand tensile forces. However, other isolation systems have also been studied, such as the IsolGOODS (Tagliaferro *et al.* 2021), whose isolation period does not depend on the mass stored. Its design is grounded on the principles of the simple pendulum, akin to the seismic isolation system utilizing curved surface sliders (CSS) (Fukahori *et al.* 1990). Maureira (2018), Álvarez *et al.* (2021), and Maureira-Carsalade *et al.* (2020) studied a rolling-type seismic isolation device. The structure moves on an isolator of semi-spherical head of radius R and height H , both connected by a pre-tensioned cable and spring. Lateral stiffness comes from the tension (T) of the cable-spring system and the structure's weight. The last only

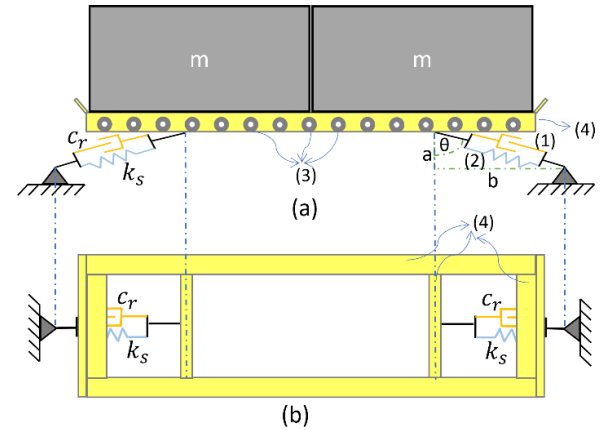


Fig. 1 Schematic model of the load-level isolation system. (a) Side view (b) Plan view

matters if H is less than the R . If the $T=0$ and $R > H$, stiffness depends solely on the structure's weight, keeping the isolation period constant.

It is well known that base seismic isolation loses effectiveness in structures with long fundamental periods. However, this issue is less pronounced with segmented or level isolation, depending on the floor where the isolation systems are located. This technique has become a valuable solution for effectively separating different parts of tall buildings, which have various purposes and, therefore, different seismic performance requirements (Forcellini and Kalfas 2023). These authors mention that this technique allows for filtering the inertial forces transmitted to the superstructure and improves its seismic performance due to the damping effects of the mass on the substructure. Several studies on buildings with segmented isolation have shown that the superstructure changes its modal properties and improves seismic performance (Davide and Konstantinos 2023, Pan and Cui 1998, Pan *et al.* 1995, Wang *et al.* 2012). For better performance using this technique, the design should aim to minimize multiple structural response parameters due to the combination of seismic isolation and mass damping (Donà *et al.* 2018). The above evidence indicates that, for slender and flexible structures, segmented isolation can be more effective than base isolation.

Similarly, the seismic isolation technique can be applied to the load level of racks to improve their overall seismic behaviour, for both new and existing applications. In particular, Donà *et al.* (2022) first investigated the effectiveness of optimal load-level isolation systems (LLIS) applied in the cross-aisle direction based on various case study racks, demonstrating that LLIS can effectively reduce upright stresses as well as load-level drifts and accelerations; subsequently, Bernardi *et al.* (2023) provided a general design method of LLIS for optimizing the seismic performance of pallet racks

Rack structures can be very flexible in the down-aisle direction (Donà *et al.* 2022). The above leads to high lateral relative deformation (*drift*) and rotation at the beam-column connection. This presents a challenge in designing such structures in seismic countries like Chile, as it is often difficult to meet maximum *drift* restrictions. Because of

this, the isolation system presented here was designed to work in the down-aisle direction, aiming to reduce floor drift.

The authors of this paper have preliminary experimental results, which will be presented in a forthcoming article, that demonstrate the benefits of implementing the load-level isolation system for down-aisle direction presented here. It was observed a significant reduction in the fundamental period in the down-aisle direction when this isolation system was implemented. Moreover, lateral displacement and base shear load were reduced when compare to the mass fixed condition. Importantly, all of these improvements were achieved without exceeding the available deformation allowance (7.5 cm) of the isolation level.

2. Conceptual and analytical model

Figs. 1(a) and 1(b) depict schematically the conceptual model of the proposed load-level isolation system. The main components of this system include: (1) dampers, (2) linear springs, (3) bearing system, and (4) rigid platform. The platform supports the load and connects with the damper-spring systems and the rack beams. A bearing system reduces shear load transfer between the platform and the rack beams, facilitating smooth movement. Linear springs operate solely in compression, functioning one at a time. However, they can also work together in a region near the system's resting state due to a pre-compression initial deformation. Dampers contribute in both, tension and compression, although their behavior may vary in each loading direction.

Fig. 2(a) displays the free-body diagram of the isolation system, illustrating all interacting forces (inertial, dissipative, elastic, weight and normal force).

Inertial forces (F_I) act on the mass placed on the isolation system due to absolute acceleration induced by earthquake.

Dissipative forces (F_{D1} and F_{D2}) are concentrated in the dampers and depend on their mechanical characteristics and deformation velocity. Another dissipative force is friction force (F_r) occurring between the isolation platform supporting the stored load and the rack beams. This force is produced due to the relative displacement of the internal components of the bearings that allow the rolling of the isolation platform on the rack beams. In Fig. 2(a) the force F_r is the projection of all friction forces on the degree of freedom of horizontal movement of the isolation platform in a single equivalent kinematic friction force. This force depends on the equivalent friction coefficient of the bearing system and the weight of the isolation platform plus the weight of the objects stored on it.

The elastic force of the isolation system can be characterized in two deformation stages. The first is the pre-compression stage, where both springs work simultaneously as long as the displacement is less than a certain threshold. That is, while $|u| < u_0$, the elastic force is provided by the sum of the stiffnesses of both springs. In the second stage, upon surpassing the aforementioned pre-compression

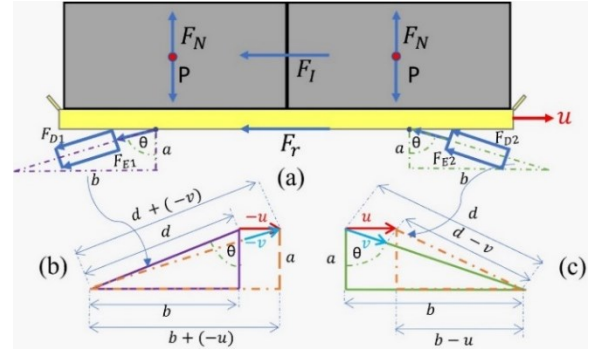


Fig. 2 Free body diagram of the pallet isolation system

threshold, the tensioned spring is completely disengaged, leaving only the compressed spring to provide stiffness to the isolation system. These springs not only supply elastic force to the device but also enable self-centering, necessitating their operation within the linear elastic range at all times.

In Fig. 2(a), the positive direction of the global degree-of-freedom (DOF) of the isolation system (u) is defined to the right. The local DOF of each damper-spring system is defined as positive when it is compressed (Fig. 2(c)). Both damper-spring systems are symmetrically arranged with respect to a vertical line that cuts the isolation system in half. Therefore, if we rotate Fig. 2(a) 180° about this line, the global DOF u would point to the left, and the left damper-spring system (Fig. 2(b)) would be on the right and compressed. The previous case would correspond to analyzing the damper-spring of Fig. 2(c), but with global DOF $-u$, having local DOF $-v$. This consideration allows defining the local DOF v of both damper-spring systems through a single kinematic relationship (Eq. (1)), taking into account that their DOFs have opposite signs due to symmetry.

$$v = d - \sqrt{(b - u)^2 + a^2} \quad (1)$$

$$d = \sqrt{b^2 + a^2} \quad (2)$$

Considering Coulomb friction force (Cull and Tucker 1999, Kelly *et al.* 2000), the force F_r of Fig. 2(a) is given by Eq. (3), with an equivalent friction coefficient μ_{eq} .

$$F_r = \mu_{eq} F_N \text{sign}(\dot{u}) \quad (3)$$

In Eq. (3), the factor “ $\text{sign}(\dot{u})$ ” denotes that the friction force opposes the relative displacement between the parts subjected to the normal force F_N .

Discontinuity functions of the isolation platform's stiffness system are proposed, which allow incorporating in its numerical model the increase in rigidity in the proximity of the rest position ($|u| < u_0$). Associated with u_0 , a spring deformation threshold $v = v_0$ is defined, by evaluating the deformation $u = u_0$ in Eq. (1). Considering the above, the discontinuity functions for the left and right springs in Fig. 2(a) are respectively defined by Eqs. (4) and (5), and the analytical model of the isolation system is defined by Eq. (6).

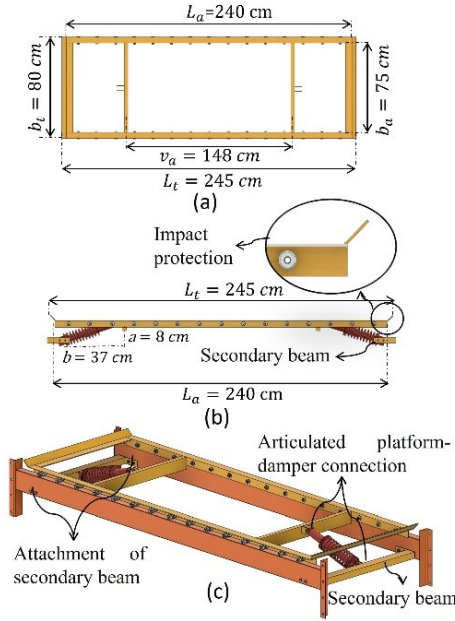


Fig. 3 Isolation system components with their dimensions. (a) Plan view (b) Side view (c) 3D view

$$f_{d1}(v) = \frac{1}{2} \cdot (1 - \text{sign}(v - v_0)) \quad (4)$$

$$f_{d2}(v) = \frac{1}{2} \cdot (1 + \text{sign}(v + v_0)) \quad (5)$$

$$F(u, \dot{u}) = k_s \cdot (v + v_0) (f_{d1}(v, v_0) + f_{d2}(v, v_0)) \cdot \sin \theta + (F_{D1}(\dot{v}) + F_{D2}(\dot{v})) \cdot \sin \theta + \mu_{eq} \cdot m \cdot g \cdot \text{sign}(\dot{u}) \quad (6)$$

where $\sin \theta$ is obtained through Eq. (7), k_s is the stiffness of each of the two springs in the system and F_{D1} , F_{D2} are the equations of the analytical model for characterizing the energy dissipation mechanism in the dampers on the left and right side of the diagram of the Fig. 2(a).

$$\sin \theta = \frac{b - u}{d - v} \quad (7)$$

$$\dot{v} = \frac{(b - u)}{\sqrt{(b - u)^2 + a^2}} \dot{u} \quad (8)$$

The local deformation rate of the spring in Fig. 2(c) is given by Eq. (8). This is used in Eq. (6) to characterize the dissipative forces F_{D1} and F_{D2} (Fig. 2(a)), whose analytical model is presented in section 3.4.

3. Experimental characterization and results

In this section, the materials, methods, and results of the experimental campaign for the characterization of the isolation system components are presented. Three different types of tests were conducted. In the first one, the equivalent friction coefficient between the isolation platform (element (4) in Fig. 1(a)) and the rack beams is



Fig. 4 Arrangement of bearings in the isolation platform

determined. The second set of tests was designed to characterize the stress-deformation behavior of the springs, which are utilized to determine the stiffness of each one. Finally, the dampers were tested and characterized under cyclic loading at different speeds. This enabled the adoption of an analytical model to characterize its energy dissipation mechanism.

3.1 Dimension and details of the isolation system

The design and construction of the isolation platform (marked as (4) in Figs. 1(a) and 1(b)) were executed by LEMUSSE, a company actively engaged in collaborative research and development efforts with the team of researchers involved in this article. The dimensions of the platform were determined considering that it needed to support a maximum storage load of 2 tons. The geometry and dimensions of the platform are shown in Figs. 3(a)-3(b). The 3D view in Fig. 3(c) shows how the isolation platform connects via the damper-spring system to the secondary beams. They are attached to the rack beams upon which the isolation platform rolls. In the zoom of Fig. 3(b)-3(c), the solution for a potential impact between the isolation platform and rack columns is shown. This consists of an L-shaped beam with a 135-degree angle between their

flanges, arranged at each end of the platform. The flange of the L that comes into contact with the column would bend, dissipating energy through metal yielding, thereby reducing the transmitted force.

Based on the observation of experimental trials of multi-level load racks on shaking table with simulated earthquakes (which are part of an ongoing research), the following can be said. Even with an isolation period of 2.5 seconds, the displacement between the isolation platform and the rack did not exceed 7.5 cm. Effective decoupling of the stored mass from the rack vibration was observed. The movement recorded in the beams supporting the loaded isolation systems was quite different from that of the rack with fixed mass. It is inferred that this, along with the damping capacity of the isolation system, is the reason for the low deformation demand placed upon it.

3.2 Platform-beam equivalent friction coefficient

The equivalent friction coefficient (μ_{eq}) is as a single friction coefficient that characterizes the energy dissipation and force of friction of the complete system. This is by means of a simplified model, which in this case is the

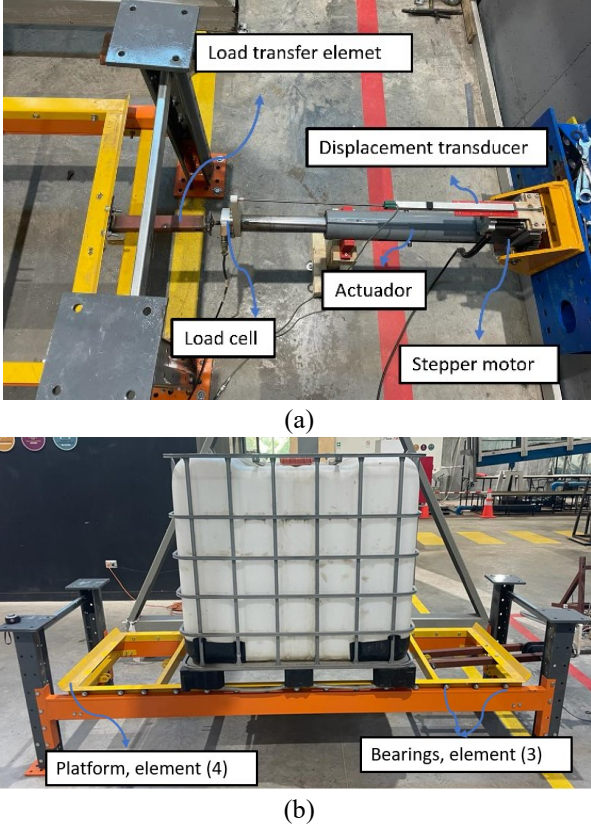


Fig. 5 Experimental set-up to determine μ_{eq} . (a) Electro-mechanical actuator and load cell. (b) Loaded isolation platform, on low rack beams

Coulomb model (Cull and Tucker 1999, Kelly *et al.* 2000). In the test defined to characterize the above, commercial bearings were used that were placed at 15 equidistant points on each side of the isolation platform, as shown in Fig. 4. The platform was drilled at each point and, using bolts, 3/8" diameter and nuts, two bearings were fastened with a nut in between to allow independent rolling. With the foregoing, the aim is to avoid exceeding the load that these bearings could support.

To obtain the equivalent kinematic friction coefficient of the system (μ_{eq}), an experimental protocol was defined, and the setup shown in Figs. 5(a) and 5(b) was built. This setup comprises a storage rack consisting of 4 short columns, each with its respective base plate anchored to the slab with bolts. Additionally, there is a pair of beams forming a low and laterally rigid frame, with the isolation platform positioned atop them, supported by bearings. Finally, a water storage ponds of 1 m³ capacity is installed on the platform to provide mass (Fig. 5(b)).

A computer-controlled electromechanical actuator powered by a stepper motor, with a maximum travel distance of 300 mm was used in the trials. A load cell with a measurement capacity of up to 2000 lbs. was installed at the end of the actuator's moving shaft to be measure the load applied to the isolation platform. This load cell was attached to an auxiliary interconnection element fixed to the isolation platform. Additionally, a displacement transducer with a 300 mm stroke was installed between the end of the

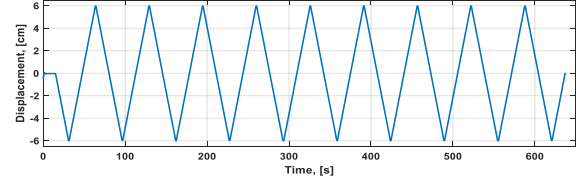


Fig. 6 Load-unload cycle for equivalent kinematic friction coefficient characterization tests

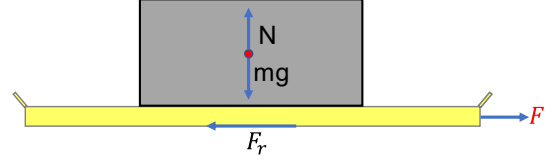


Fig. 7 Free body diagram of the isolation platform with added mass subjected to side loading

actuator's moving shaft and its body, allowing for the displacement imposed on the isolation platform to be measured.

The sequence imposed by the actuator corresponds to that shown in Fig. 6, which consists of 10 cycles of sawtooth type with constant amplitude (6 cm) and velocity (1.5 mm/s).

Fig. 7 illustrates the free body diagram (FBD) of the isolation platform with additional mass on it. This was used to determine the equivalent friction coefficient between the platform and the beams (Eq. (9)). Where m corresponds to the total mass, that is, the added mass plus the mass of the isolation system considering all its components (38 kg).

$$F_r = \mu_{eq} \cdot m \cdot g \quad (9)$$

Fig. 8 shows the force-deformation curves of the load-unload cycles corresponding to each conducted test. These were carried out with different masses (in red: 790 kg and blue: 1,796 kg), each repeated three times (in separate graphs). The weights were determined by suspending the objects from a crane frame using a digital scale on the suspension cable. In all the curves of Fig. 8, it is evident that after the relative movement begins and the kinematic friction force starts to act (F_r in Fig. 7 and Eq. (9)) both in the load-unload branches, said force remains practically constant. However, a bigger friction force is observed when the movement changes direction, which is due to the deformation speed is zero for a short time, there being a static force that must be overcome.

The data presented in Fig. 8 were processed to obtain the average dissipated energy \bar{E}_d of the $N_c=10$ load-unload cycles of each of the $N_T=6$ experimental trials carried out (Eq. (10)). The energy dissipated by cycle is the area inside the force-deformation closed curve in each load-unload cycle ($C_i, i = 1, \dots, N_c$).

$$\bar{E}_d = \frac{1}{N_c} \sum_{i=1}^{N_c} \oint_{C_i} F du \quad (10)$$

The average dissipated energy (\bar{E}_d) allows to determine an equivalent friction coefficient (μ_{eq}) associated with a

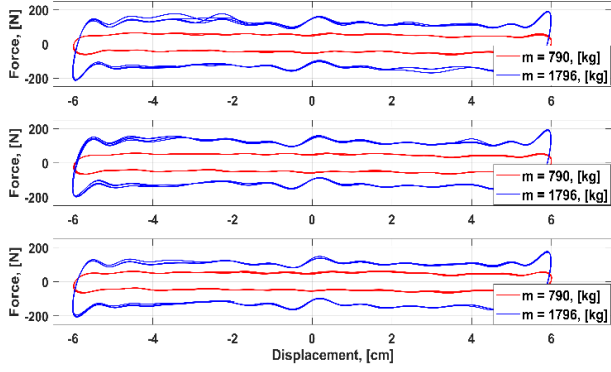


Fig. 8 Cyclic force-deformation curves of the platform-mass system sliding on the rack support beams

Coulomb friction model given by Eq. (9). Considering that the forcing is a cyclic deformation of amplitude u_{max} , and equating the dissipated energy calculated with Eq. (10) with that obtained from a Coulomb friction model ($E_d = 4F_r u_{max}$) the equivalent friction coefficient is obtained from the average of the $N_c = 10$ load-unload cycles (Eq. (11)).

$$\mu_{eq} = \frac{\bar{E}_d}{4mg u_{max}} \quad (11)$$

The results of \bar{E}_d and μ_{eq} per test are shown in Table 1, indicating at the end the simple average of the equivalent friction coefficients of each test ($\bar{\mu}_{eq}$). This corresponds to the isolation platform-beam friction coefficient of the calibrated system.

The low magnitude of $\bar{\mu}_{eq}$ is due to the bearings system that facilitates the relative displacement between the isolation platform and the support beams of the rack. Between the bearings and the support beams, sliding does not occur, but rolling. Sliding and friction occurs internally in the parts that make up the bearings, which are designed to minimize the effect of friction. Therefore, it can be said that the bearings fulfill the function of allowing a fluid movement of the isolation platform on the support beams. This allows concentrating the dissipation of energy in the dampers that connect the isolation platform with the rack structure.

3.3 Characterization of the springs

The springs used are coil springs made with cylindrical steel bars that work solely in compression. Since an economical vehicle shock absorber was used in parallel with the spring, his design took into consideration the geometric constraints imposed by the chosen shock absorber. Due to the above, the spring must have a length shorter than that of the damper, defined as d , in Figs. 2(b)-2(c). The bar diameter and number of spring coils were chosen taking into account two conditions. The first is that it can operate within the elastic linear range throughout the allowable deformation range of the isolation system. The second is that the isolation system, loaded with the maximum capacity of the rack per level (2000 kg), has a

Table 1 Experimental results of the coefficient of friction

Test No.	mass, m (kg)	Average Dissipated energy, \bar{E}_d (J)	Eq. coefficient of friction, μ_{eq}
1	790	13.34	0.0072
2	790	13.15	0.0071
3	790	13.45	0.0072
4	1796	30.35	0.0072
5	1796	33.87	0.0080
6	1796	31.89	0.0075
Average equiv. coefficient of friction			$\bar{\mu}_{eq} = 0.0074$

period of 2.5 seconds. This is adequate to significantly reduce the transmission of inertial forces between the fully loaded pallet and the rack.

The stiffness of the spring is calculated using Eq. (12), derived from the dynamics of a linear single-degree-of-freedom system, $\omega = 2\pi/T_1 = \sqrt{k/m}$.

$$k_s = 4\pi^2 \frac{m}{T_1^2} \quad (12)$$

In this paper, only one set of springs was considered in the experimental and numerical analyses of the proposed isolation system, based on two criteria. The first is that the focus of this paper is on proposing the isolation system, its constitutive equation, determining its parameters, and validating it with experimental tests. The second is that the problem that this proposed load-level isolation seeks to address is compliance with floor drift requirements in the Chilean design regulations. To achieve the latter, it is necessary to reduce the transmission of inertial forces from the pallets to the rack structure compared to the design condition at full storage capacity. This can be achieved with full load on the pallet and a long isolation period (2.5 seconds in this case), or with reduced load and a shorter isolation period. In the second case, the effectiveness of the isolation system is lower than in the first in terms of reducing the absolute acceleration of the mass. However, in both cases, there will be a significant reduction in the force transmitted to the rack compared to its design condition at full load.

The stiffness of the spring can also be calculated using equations of the mechanics of solids with linear elastic behavior subjected to small deformations (Eq. (13)).

$$k_s = \frac{d_w^4 \cdot G}{8 \cdot D^3 \cdot N_a} \quad (13)$$

In Eq. (13), d_w is the diameter of the steel wire or bar with which the spring is made, G is the shear modulus of the material, N_a is the number of active turns in the deformation of the spring, and D is the mean diameter of the spring turn defined as the outside diameter of the coil minus the diameter of the bar.

By equating Eqs. (12) and (13), assuming the parameters m , T_1 , d , G and D are known or preset, the number of active turns required for the spring to meet the desired stiffness condition is determined (Eq. (14)).

Table 2 Parameters used in the design of the springs

Variable	G	D	d_w	N_a	k_s
unit	MPa	(mm)	(mm)	-	N/mm
magnitude	$7.96 \cdot 10^4$	79	9	10	13.24

Table 3 Experimental results of springs

Test No.	Spring No.	Experimental stiffness, $k_s^{(E)}$ (N/cm)	Exp. average stiffness, $\bar{k}_s^{(E)}$ (N/cm)	Analytical stiffness, $k_s^{(A)}$ (N/cm)	Relative error, ϵ_k (%)
1	1	139.5		132.4	
2	1	139.5	139.6	132.4	5.4
3	1	139.8		132.4	
4	2	136.8		132.4	
5	2	137.2	137.1	132.4	3.5
6	2	137.3		132.4	

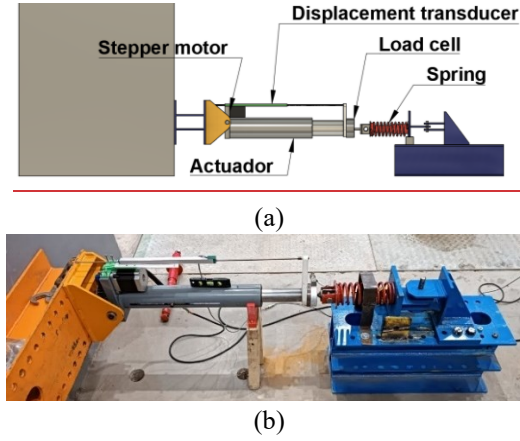


Fig. 9 Experimental test to determine spring stiffness. (a) Schematic model of the setup. (b) Photograph of the setup carried out

$$N_a = \frac{d_w^4 \cdot G}{8 \cdot D^3 \cdot k_s} \quad (14)$$

The parameters used in the design of the spring are detailed in Table 2. The spring obtained complies with the technical specifications necessary for its proper functioning in the isolation system.

In Figs. 9(a) and 9(b) the experimental setup defined to determine the actual stiffness of the designed spring is shown. A head was made that connects to the spring via compression contact, which is then linked to the installed load cell (Fig. 9(b)). The setup utilizes the same electromechanical actuator, sensors, and acquisition system that were previously mentioned in section 3.2. The movement sequence applied to the spring consisted of 10 saw-type load-unload cycles with an amplitude of 8 cm and a constant deformation speed of 2.5 mm/s. During this experimental campaign, two different springs were tested, with each test repeated three times to enhance result reliability.

Each column in the graphs of Fig. 10 represents the results of a spring, while each row shows the results of test

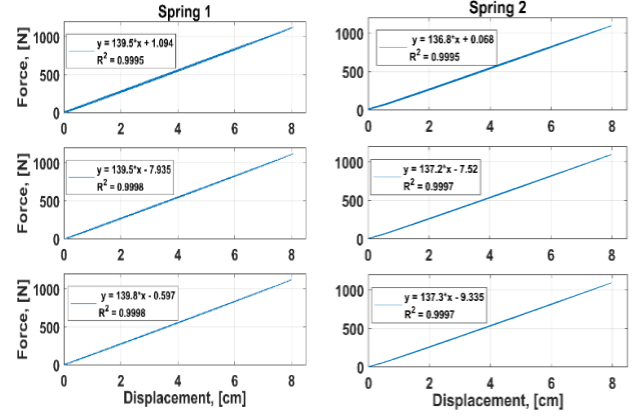


Fig. 10 Results of the load-deformation tests, with linear equation adjustment

repetitions. It was observed that both springs remained in the linear elastic range when subjected to a compression deformation of 8 cm. Table 3 summarizes the results obtained from Fig. 10, as well as the error between the expected (theoretical) stiffness and the experimentally obtained stiffness. This error was calculated using Eq. (15).

$$\epsilon_k = \frac{|k_s^{(A)} - \bar{k}_s^{(E)}|}{k_s^{(A)}} 100\% \quad (15)$$

3.4 Characterization of dampers

All the dampers used in the subsequent tests were experimentally characterized to determine their force-displacement-velocity and energy dissipation mechanism, in order to adjust an ad-hoc analytical model. The tests used dampers typically used in vehicles. An electromechanical actuator with computer-controlled displacement was used, which is an original design by the co-authors of this article. The actuator is driven by a stepper motor, which is connected to a 16 mm diameter ball screw with a pitch of $p=4$ mm/rev, capable of achieving movement sequences with a precision of 0.02 mm/step. The instrumentation scheme includes a load cell with capacity of 2000 lbs, installed at the movable end of the actuator. An inductive displacement transducer with a 200 mm stroke was installed between the fixed body of the actuator and the end of its movable shaft. The experimental setup is shown in Figs. 11(a) and 11(b).

As can be seen in Fig. 11, the dampers were tested with the same inclination as they are installed in the schematic model of the isolation system in Fig. 1, using the dimensions "a" and "b" from Figs. 3(a) and 3(b). This inclination is because the manufacturer specifies that the chamber on the fixed side of the shock absorber contains a fluid that allows dissipation but partially filled with fluid. With the above, we seek to replicate the behavior that the damper would have when installed in the isolation system.

The lateral displacement u , imposed by the actuator on the damper and measured by the displacement transducer, is projected to the local degree of freedom v by the

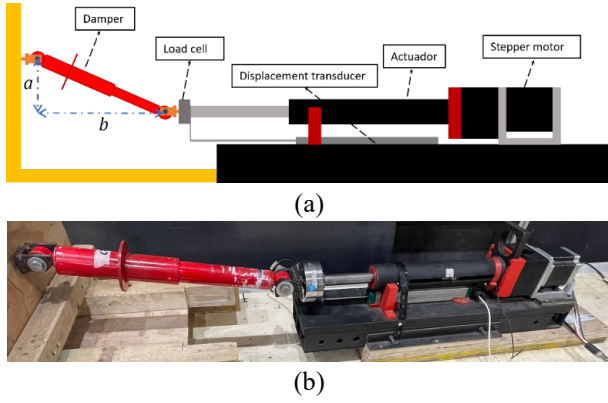


Fig. 11 Experimental setup to characterization of dampers. (a) Schematic model (b) Photograph of the setup

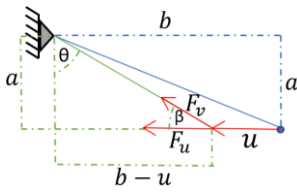


Fig. 12 Schematic model of the projection of the lateral force on the load cell to local degree of freedom v

kinematic relation of Eq. (1). On the other hand, the force measured by the load cell in the lateral degree of freedom u is also projected to the local degree of freedom v of the damper by means of Eq. (16), which uses the nonlinear kinematic relationship given by Eq. (17). Both equations arise from the geometric analysis of the schematic model shown in Fig. 12.

$$F_v = F_u \cos \beta \quad (16)$$

$$\cos \beta = \frac{b - u}{\sqrt{(b - u)^2 + a^2}} \quad (17)$$

The load-unload cyclic deformation sequence to which the dampers were subjected consists of a saw-type signal of 10 cycles, similar to Fig. 6, but with an amplitude of 8 cm, and varying the deformation velocity. The choice of this amplitude was because when the complete isolation system is in operation, the damper can work both in tension and compression with a maximum amplitude of $u=7.5$ cm. This deformation corresponds to the clearance between the side edges of the isolation platform and the inside faces of the rack columns. Due to the above, in the execution of the tests the shock absorbers were compressed up to half of their maximum stroke, this being the null deformation condition ($u=0$ in Fig. 12). From this condition, each of the experimental tests began applying the deformation sequence described above. Two shock absorbers of the same type were tested, each of them subjected to 6 different speeds of deformation (5.3, 6.8, 9.5, 12.8, 15.1 and 17 mm/s). The selection of these speeds was restricted by the actuator used, seeking to use it to its full capacity.

Fig. 13 displays the load-unload cycles of each damper, where the positive branch corresponds to tensile load and

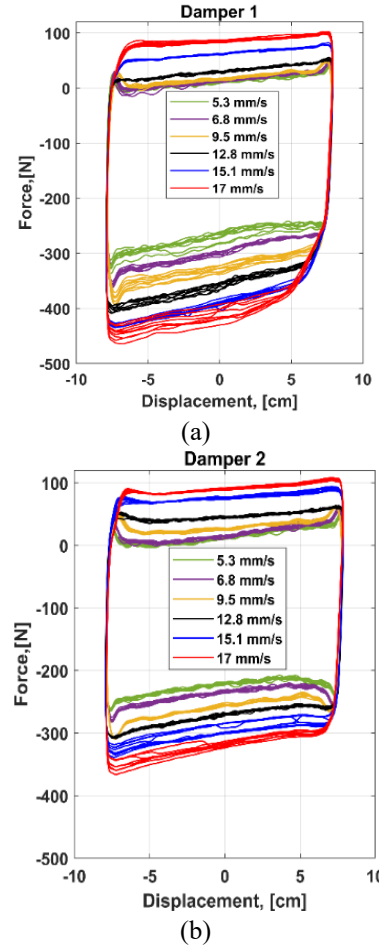


Fig. 13 Hysteresis cycles of tested dampers. (a) Damper 1. (b) Damper 2

the negative branch is compression. Upon analyzing the results, it can be observed that the dampers used do not exhibit the typical viscous behavior; rather, they show a behavior more akin to a frictional dissipator with velocity dependence. Based on the results, it can be stated that the dampers have a fairly stable behavior between successive load-unload cycles, as each test with the same velocity underwent 10 cycles, which overlap relatively well.

Fig. 14 show the results of average dissipated energy per cycle of each one of the tests, which was calculated using Eq. (10), for all the strain rates studied. In said figure, the legend refers to the results of Table 4, so that DX- RY refers to the Damper N° X with data from Repetition N° Y of the test, and DX-Av corresponds to the Damper N° X with the average results of the repetitions.

Fig. 15 and Table 4 show the results of the maximum (compressive) and minimum (tensile) forces obtained from the post-processing of the tests carried out on the two dampers. Figs. 15(a) and 15(b) show the average maximum forces of the loading branch (compression) and the unloading branch (tension) respectively. The average maximum force was calculated for both the compression and tension branch. It is the average of the responses of the $N_c=10$ cycles of each test in a window up to $N_u=0.8$ times the maximum amplitude of imposed deformation (Eq. (18)).

Table 4 Parameters of the equation fitted to the average of the maximum forces in compression and tension

Trials	Compression			Tension			R^2
	s , (N·s/m)	c , (N)	R^2	g (N·s/m ²)	s , (N·s/m)	c , (N)	
Damper. N°1, Average	$s_{1,c}^{(av)} = -11,110$	$c_{1,c}^{(av)} = -224.1$	0.968	$g_{1,t}^{(av)} = 736.9$	$s_{1,t}^{(av)} = -9,932$	$c_{1,t}^{(av)} = 40.9$	0.995
Damper. N° 2, Average	$s_{2,c}^{(av)} = -7,865$	$c_{2,c}^{(av)} = -188.4$	0.987	$g_{2,t}^{(av)} = 560.9$	$s_{2,t}^{(av)} = -5,095$	$c_{2,t}^{(av)} = 20.9$	0.996

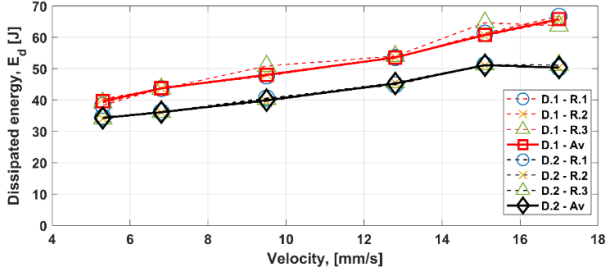
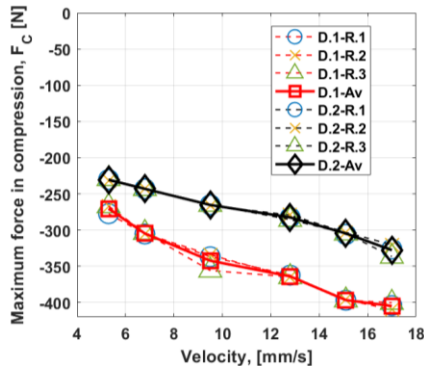
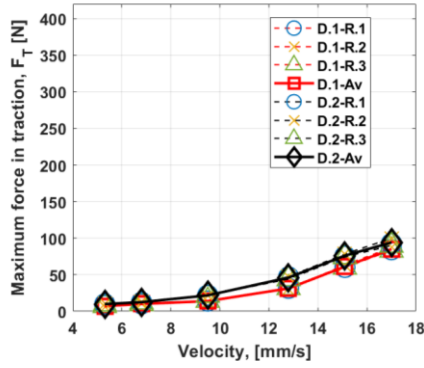


Fig. 14 Dissipated energy of the three tests carried out on each damper and their respective average curves



(a)



(b)

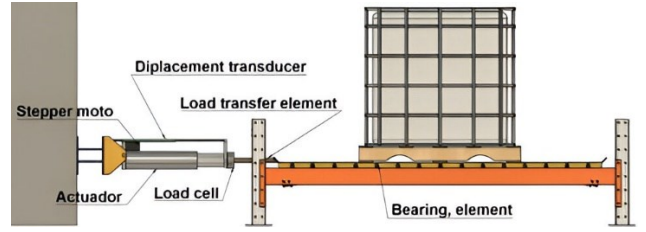
Fig. 15 Maximum forces in cyclic shock absorber tests. (a) Compression, (b) Tension

$$\bar{F}_{t,c}^{max} = \frac{1}{N_c} \sum_{i=1}^{N_c} \left(\frac{1}{2N_u u_{max}} \int_{-N_u u_{max}}^{N_u u_{max}} \frac{1 \pm \text{sign}(F^{(i)})}{2} F^{(i)} du \right)_{i-th \text{ cycle}} \quad (18)$$

In Fig. 15(a) an approximately linear dependence of the average maximum compression force with respect to the deformation velocity of the test can be observed. On the other hand, in Fig. 15(b) it can be seen that the maximum tensile force of the shock absorbers has an approximately



(a)



(b)

Fig. 16 Experimental setup for characterization tests of the pallet isolation. (a) Photograph (b) Schematic model

quadratic dependence with respect to the deformation speed of the test. There is also evidence of a difference in the maximum forces of each dampers. The response of the first tested damper being greater compared to the second. However, this difference is less than that observed between the maximum compressive and tensile forces. Finally, when comparing the magnitude of the maximum forces in compression and tension, it can be observed that, regardless of the test speed, the response of the shock absorber is greater when it is working in compression than in tension.

Functions were fitted to the experimental results from Figs. 15(a)-15(b). Linear fits ($y = s \cdot x + c$) were applied to the data from Fig. 15(a), while quadratic fits ($y = g \cdot x^2 + s \cdot x + c$) were used for the data from Fig. 15(b). The parameters of the fitted functions were obtained by minimizing the mean squared error between experimental results and fitted function. These parameters, along with their correlation coefficients R^2 , are shown in Table 6.

Based on the fitting equations, whose parameters are detailed in Table 4, analytical models were defined to characterize the energy dissipation mechanism in the dampers on the left (F_{D1}) and right (F_{D2}) side of Figure 1 (a), in accordance with Eq. (6). These analytical models are represented by Eqs. (19) and (20), respectively.

$$F_{D1} = \left(g_{1,t}^{(av)} \cdot \dot{v}^2 + s_{1,t}^{(av)} \cdot \dot{v} + c_{1,t}^{(av)} \right) \cdot f_{a1}(\dot{u}) + \dots + \left(s_{1,c}^{(av)} \cdot \dot{v} + c_{1,c}^{(av)} \right) \cdot f_{a2}(\dot{u}) \quad (19)$$

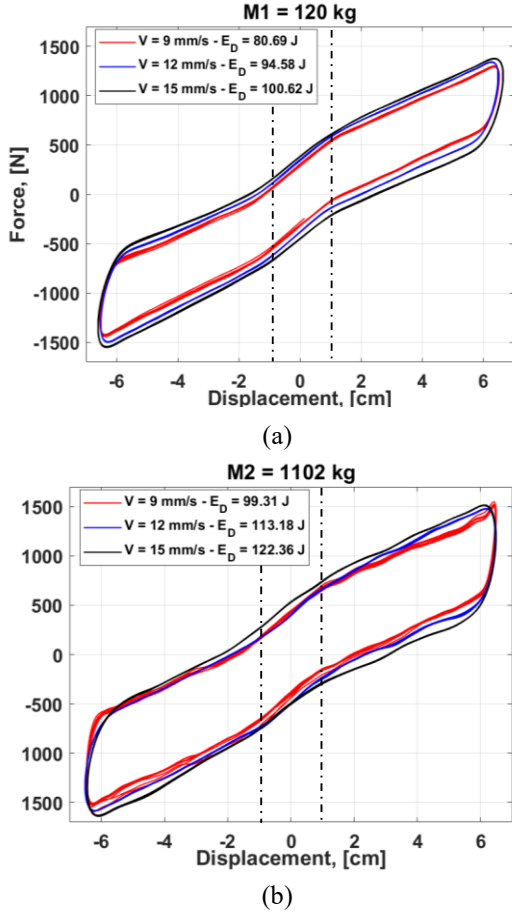


Fig. 17 Load-unload cycles of the isolation system. (a) with a mass of 120 kg (b) with a mass of 1.102 kg

$$F_{D2} = (g_{2,t}^{(av)} \cdot \dot{v}^2 + s_{2,t}^{(av)} \cdot \dot{v} + c_{2,t}^{(av)}) \cdot f_{a2}(\dot{u}) + \dots \quad (20)$$

$$\dots + (s_{2,c}^{(av)} \cdot \dot{v} + c_{2,c}^{(av)}) \cdot f_{a1}(\dot{u})$$

Where $f_{a1}(\dot{u})$ and $f_{a2}(\dot{u})$ are activation functions that assume a value of 0 or 1 and sum to 1. They define whether the compression or tension branch of each damper is working. Note that these functions also impose the condition that when one damper works in tension the other works in compression, as evidenced by analyzing Eqs. (21) and (22).

$$f_{a1}(\dot{u}) = \frac{1}{2}(1 + \text{sing}(\dot{u})) \quad (21)$$

$$f_{a2}(\dot{u}) = \frac{1}{2}(1 - \text{sing}(\dot{u})) \quad (22)$$

The dampers were tested at various speeds, all of which were relatively low compared to those experienced during earthquakes. While the tested dampers contain fluid in one of its chambers, it is not full. This was evidenced from the experimental results, as behavior was observed more akin to that of a frictional damper than a viscous one, with a slight speed dependency. Furthermore, the actuator used in the experimental tests was limited by a maximum loading rates of 17 mm/s.

3.5 Characterization of the isolation system

The behavior of the complete insulation system subjected to a sequence of cyclical forced deformation was characterized in order to verify the fidelity of the analytical characterization model presented above. The experimental setup uses the same electromechanical actuator, displacement transducer and load cell described in section 3.1, but a rigid transmission element is added between the load cell and the isolation platform (Figs. 16(a) and 16(b)). However, in this case the transmission gears between the motor and the spindle were changed to achieve a push/pull according to the numerical predictions, restricting the maximum strain rate imposed to 15 mm/s.

The cyclic load-unload deformation sequence to which the isolation system was subjected consists of a saw-tooth signal of 10 cycles, similar to the one shown in Figure 6, but with an amplitude of 6.5 cm and different deformation speeds. A 1 cm gap was left between each edge of the isolation platform and the inside face of the rack columns to prevent impact between both elements and thus protect the equipment used. The deformation imposed by the actuator was applied at three different speeds: 9, 12, and 15 mm/s. Tests were conducted with two different masses on the isolation platform (120 kg and 1,102 kg including isolation platform). Tests with larger masses could not be performed due to the actuator's limitation in speed-loading capacity. Tests were carried out for all the combinations of deformation speed and mass described above (in total 18 tests), repeating each test 3 times for greater reliability.

Fig. 17 shows the results of the tests described earlier. Within the dash-dot lines, both springs work in compression, but outside of them, only one works. Based on these results, it can be said that increasing the mass on the isolation platform slightly increases the maximum force with which the isolation system responds, and the energy dissipated per cycle. This increase is slight due to the low equivalent coefficient of friction between the isolation platform and the support beams, so the force with which the isolation system reacts is strongly controlled by the damper-spring systems. On the other hand, increasing the deformation speed also results in a slight increase in the energy dissipated per cycle and the force with which the isolation system responds. This is due to the dependence of the damper force on the imposed deformation velocity is low. Therefore, it can be said that there is a clear agreement between the results of the dampers alone and those of the complete isolation system. Regarding the elastic force of the isolation system, two branches with different slopes can be observed in the experimental results. This indicates the joint work of the two springs near the rest position, but only one of them functions beyond a certain deformation threshold of approximately ± 1 cm. This is consistent with the proposed analytical model developed in section 2 and Eq. (6).

4. Validation of the model with experimental results

The analytical model of the isolation system defined by

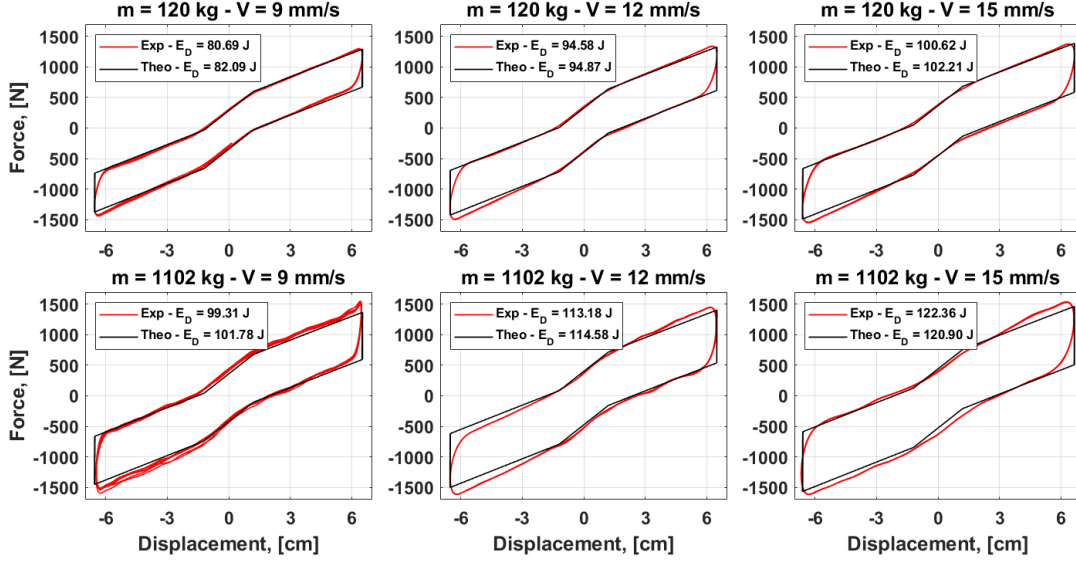


Fig. 18 Comparison of hysteresis loops with different masses and speeds obtained experimentally and numerically

Table 5 Relative errors of the energy and force obtained experimentally and theoretically

Test No.	mass, m (kg)	Deformation velocity (mm/s)	Experimental dissipated energy (J)	Theoretical dissipated energy (J)	Relative Error (%)	
					ϵ_{E_d}	ϵ_F
1	120	9	80.69	82.09	1.71	5.95
2	120	12	94.58	94.87	0.31	6.98
3	120	15	100.62	102.21	1.56	8.03
4	1102	9	99.31	101.78	2.43	8.17
5	1102	12	113.18	114.58	1.22	9.98
6	1102	15	122.36	120.90	1.21	9.57

Eq. (6) was programmed in Matlab with calibrated parameters based on the results from sections 3.2 to 3.4. The calibrated analytical model combines Eqs. (4) to (6) and (19) to (22) with the results shown in Tables 5. The experimental results used to calibrate the analytical model are independent of those of the section 3.5, with which the numerical results were compared for validation.

In Fig. 18, the experimental results superimposed with those obtained using the calibrated analytical model are presented. The graphs in each column represent they share the same strain rate, but with different masses. Plots in the same row show results with the same mass, but different strain rates. Within each graph, the results obtained experimentally are shown in red, while those obtained with the calibrated analytical model are shown in black. Each legend indicates the value of the energy dissipated in a complete load-unload cycle of each test configuration obtained experimentally and numerically. It is observed that the increase in the dissipated energy calculated both numerically and experimentally is directly related to the increase in deformation speed and mass. Finally, it can be said that in all the graphs presented there is a very good similarity between the experimental and numerically obtained curves. This allows validating the analytical model in reproducing the behavior of the isolation system.

The dissipated energy results presented in the legends of Fig. 18 are shown in Table 5. These results were used to calculate a relative error between the calculations based on

experimental results and those obtained by means of the analytical model (Eq. (23)). When analyzing this relative error, it can be said that there is a very good fit between the analytical model, relative to the experimental results, with errors below 2.5%.

$$\epsilon_{E_d} = \frac{\left| \overline{E_d^{(Ex.)}} - \overline{E_d^{(A.M.)}} \right|}{\overline{E_d^{(Exp)}}} 100\% \quad (23)$$

A relative error was also calculated to quantify the appropriate fitting in predicting the force with which the isolation system responds. It evaluates the mean relative difference of force between the predictions using the analytical model and experimental results (Eq. (24)), based on the error proposed by Maureira-Carsalade *et al.* (2021). The results of these calculations are presented in Table 5, allowing the validation of the numerical model by confirming its capability not only to replicate the energy dissipation capacity but also to estimate the force with which the isolation system responds, with a relative error less than 10%.

$$\begin{aligned} \epsilon_F &= \frac{\frac{1}{N_c} \sum_{i=1}^{N_c} \phi \left| (F^{(Ex.-i)} - F^{(A.M.)}) u du \right|}{\frac{1}{N_c} \sum_{i=1}^{N_c} \phi |F^{(Ex.-i)} u du|} 100\% \\ &= \frac{\frac{1}{N_c} \sum_{i=1}^{N_c} \phi \left| (F^{(Ex.-i)} - F^{(A.M.)}) u \dot{u} \right| dt}{\frac{1}{N_c} \sum_{i=1}^{N_c} \phi |F^{(Ex.-i)} u \dot{u}| dt} 100\% \end{aligned} \quad (24)$$

5. Numerical implementation of the isolation system

The dynamic equilibrium equation of a mass on the isolation system presented here, located on a rack with assumed infinite stiffness, was programmed in MATLAB (Eq. (25)). The system is a single-degree-of-freedom (u) and describes the interaction between the inertial force induced by ground motion ($\ddot{u}_g(t)$) and the response of the isolation system, $F(u, \dot{u})$. The latter is defined by Eq. (6), with parameters calibrated with the experimental results of each of the device components.

$$m(\ddot{u} + \ddot{u}_g) + F(u, \dot{u}) = 0 \quad (25)$$

Eq. (25) does not consider the elastic and the dissipative force separately since both are contemplated in the nonlinear force $F(u, \dot{u})$. The differential Eq. (25) was solved for two different masses, 1000 and 2000 kg, including isolation platform and mass on top of it.

The seismic forcing $\ddot{u}_g(t)$ (Fig. 19 (a)) corresponds to one of the horizontal components of the earthquake of February 27, 2010, measured at the San Pedro de la Paz station. Said component was scaled in the frequency domain to adjust its response spectrum with the design spectrum of NCh2369, in type C soil, seismic zone 3, with an importance factor of the structure $I=1$ and a reduction factor of the response $R=1$ (Fig. 19(b)).

Fig. 20 shows the results of the non-linear dynamic analysis given by Eq. (25). The responses include the displacement of the pallet relative to the supporting beams of the very stiff rack, as well as the absolute acceleration of the pallet. From Fig. 20 and Table 6, it can be observed that for both masses, there is a reduction in absolute acceleration, and the displacement range available for the isolation system (7.5 cm) is not exceeded. Clearly, the reduction in absolute acceleration is greater for a 2-ton mass than for a 1-ton mass, as the stiffness remains constant. This leads to an isolation period of 2.5 seconds for full storage capacity, with the period decreasing when the mass is reduced. While this might seem inefficient at first glance if one aims to maximize the reduction in absolute acceleration, it turns out to be beneficial from a design perspective. In Table 6, the shear load transmitted by the stored mass to its base is compared between the condition with pallet isolation versus the case with fixed mass. Considering the design shear of the rack at full capacity with fixed mass ($Q_{0,max}^{(fixed)}(full)$), the shear transmitted by the isolation system with mass m upon it ($Q_{0,max}^{(I.S.)}(m)$) is lower than that of the design with fixed mass. This occurs in both cases, with mass $m=2$ Ton and with mass $m=1$ Ton upon the isolation platform. Therefore, while reducing the period decreases the effectiveness in reducing absolute acceleration, when combined with a lower mass, it results in a reduced transmission of shear force. In the example shown, the transmission of shear force is lower for the case of reduced mass with isolation, compared to the condition of full mass, both fixed to the rack and seismically isolated (Table 6).

This section is just an example of using the constitutive equation of the proposed isolation system, with parameters

previously calibrated using experimental results, to determine the response of a simple system subjected to seismic loading. This example does not seek to demonstrate the efficiency of the proposed isolation system in industrial rack usage scenarios, nor does it aim to establish optimal design conditions for racks incorporating it. The optimization of such designs is a more complex task that depends on the characteristics of the rack, the isolation system, and the positions in which it is installed (Bernardi *et al.* 2023). The aforementioned, as well as the incorporation of bi-directionality in the isolation system, are research lines currently being developed by the co-authors of this paper.

6. Conclusions

An analytical model capable of predicting the response of the proposed pallet (or load-level) isolation system was formulated. The parameters of the analytical model were then calibrated using experimental results that allowed the separate characterization of the individual behavior of the isolation system components. The response of the analytical model was compared with experimental tests of the complete isolation system. In both cases, the same sequence of displacement of the isolated DOF was considered as external forcing. The experimental response of the complete isolation system is independent of those obtained for the characterization of individual device components and used to calibrate analytical model. This allowed for a double-blind validation of the predictive analytical model. It was verified its accuracy in reproducing both the force with which the system responds to an imposed excitation (with an error of less than 10%) and its energy dissipation capacity (with an error of less than 3%). The calibrated analytical model was used to obtain the dynamic response of the pallet isolation system subjected to a seismic excitation. The results demonstrated that the isolation system is self-centered, it is effective to reduce de absolute acceleration of the mass, and the shear load transmitted to the supports of the isolation system. Moreover, the maximum allowable deformation of the isolation system (7.5 cm) is adequate for it to operate effectively without impacting adjacent columns.

The load level isolation system presented in this research was tested with specific damping and isolation periods, which are not necessarily suitable for all types of racks and configurations. The focus of this research was on the proposal of the system, experimental characterization, and validation of the analytical model that describes its behavior. A future research will aim to study the optimization of the parameters for different racks sizes, number of load levels and distributions of masses. Additionally, the number of isolation systems and their distribution in the rack will be analyzed, as well as their validation in a relevant environment through full-scale shake table tests.

Financing

This research was supported by the ANID FONDEF IDEA 2022 ID22I10140 project, entitled "Seismic protection of industrial storage racks through the implementation of an energy dissipation device using an inertial mass isolation". The authors also appreciate the financing granted by the company "LEMUSSE Desarrollo e Ingeniería SpA", who provided the materials and prototypes for the execution of experimental tests, in addition to a maintenance scholarship for the engineer and master's student in civil engineering Marcelo Sanhueza.

Acknowledgments

The authors thank the manager of the company "LEMUSSE Desarrollo e Ingeniería SpA", engineer Christian Leva, for his constructive comments suggested from a commercial point of view and industrial use of technology that allowed to improve this research work. The authors are also grateful to the DI-FMEI 06/2023 fund, granted by the Research Directorate of the Universidad Católica de la Santísima Concepción, Concepción, Chile.

References

- Alhan, C. and Gavin, H.P. (2005), "Reliability of base isolation for the protection of critical equipment from earthquake hazards", *Eng. Struct.*, **27**(9), 1435-1449.
- Álvarez, O., Maureira, N., Nuñez, E., Sanhueza, F. and Roco-Videla, Á. (2021), "Numerical study on seismic response of steel storage racks with roller type isolation", *Metals*, **11**(1), 158.
- Beattie, G.J. (2006), "A design guide for high level storage racking with public access", In NZSEE Conference, 8.
- Bernardi, E., Donà, M., Tan, P. and da Porto, F. (2023), "Optimal design method of the load-level isolation system for industrial steel racking", *J. Construct. Steel Res.*, **210**, 108096.
- Brown, C., Stevenson, J., Giovinazzi, S., Seville, E. and Vargo, J. (2015), "Factors influencing impacts on and recovery trends of organizations: Evidence from the 2010/2011 Canterbury earthquakes", *Int. J. Disaster Risk Reduct.*, **14**, 56-72.
- Crosier, J., Hannah, M. and Mukai, D. (2010), "Damage to steel storage racks in industrial buildings in the darfield earthquake", *Bull. New Zealand Soc. Earthq. Eng.*, **43**(4), 425.
- Cull, S.J. and Tucker, R. (1999), "On the modeling of Coulomb friction", *J. Phys. A: Mathem. General*, **32**(11), 2103.
- Donà, M., Bernardi, E., Zonta, A., Ceresara, M. and da Porto, F. (2022), "Effectiveness of load-level isolation system for pallet racking systems", *Front. Built Environ.*, **148**.
- Donà, M., Bizzaro, L., Carturan, F. and da Porto, F. (2019), "Effects of business recovery strategies on seismic risk and cost-effectiveness of structural retrofitting for business enterprises", *Earthq. Spectra*, **35**(4), 1795-1819.
- Federal Emergency Management Agency FEMA 460 (2005), *Seismic Considerations for Steel Storage Racks Located in Areas Accessible to the Public*. Federal Emergency Management Agency, Washington, D.C.
- Ferrari, M. (2019), "Lokibase: The device for seismic isolation of pallet racking systems", *Costruzioni Metalliche*, **3**, 82-91.
- Filiatrault, A., Higgins, P.S., Wanitkorkul, A., Courtwright, J.A. and Michael, R. (2008), "Experimental seismic response of base isolated pallet-type steel storage racks", *Earthq. Spectra*, **24**(3), 617-639.
- Forcellini, D. and Kalfas, K.N. (2023), "Inter-story seismic isolation for high-rise buildings", *Eng. Struct.*, **275**, 115175.
- Franco, A., Massimiani, S. and Royer-Carfagni, G. (2015), "Passive control of steel storage racks for parmigiano reggiano cheese under seismic accelerations", *J. Earthq. Eng.*, **19**(8), 1222-1259.
- Fukahori, Y., Kojima, H., Ogino, A., Suzuki, S. and Yoshizawa, T. (1990), "US Patent No. 4,899,323. Washington, DC: US Patent and Trademark Office.
- Gutelius Jr, J.B., McIntosh, S.C. and Notohardjono, B.D. (2000), US Patent No. 6,059,251.
- HClifton, C., Bruneau, M., MacRae, G., Lion, R. and Russell, T.O. (2011), "Steel structures damage desde the Christchurch earthquake series of 2010 and 2011", *Bull. New Zealand Society Earthq. Eng.*, **44**(4), 297-318.
- Kelly, R., Llamas, J. and Campa, R. (2000), "A measurement procedure for viscous and coulomb friction", *IEEE Transact. Instrument. Measurement*, **49**(4), 857-861.
- Kilar, V., Petrovčič, S., Koren, D. and Šilih, S. (2013), "Cost viability of a base isolation system for the seismic protection of a steel high-rack structure", *Int. J. Steel Struct.*, **13**, 253-263.
- Liu, Y., Wu, J. and Donà, M. (2018), "Effectiveness of fluid-viscous dampers for improved seismic performance of inter-storey isolated buildings", *Eng. Struct.*, **169**, 276-292.
- Maureira-Carsalade, N., Balboa-Constanzo, E., Sanhueza-Cartes, M., Sanhueza, C., Nuñez, E. And Roco-Videla, Á. (2023), "Proof of concept and preliminary validation of an analytical model of an energy dissipator for tension loads with self-centering capacity", *Buildings*, **13**(3), 726.
- Maureira-Carsalade, N., Pardo, E., Oyarzo-Vera, C. and Roco, A. (2020), "A roller type base isolation device with tensile strength", *Eng. Struct.*, **221**, 111003.
- Maureira-Carsalade, N., Villagrán-Valenzuela, M., Sanzana-Jara, D. and Roco-Videla, A. (2021), "Proof of concept of a novel frictional shock absorber; analytical model and experimental analysis", *Eng. Struct.*, **230**, 111657.
- Maureira, N. (2018), Patent application No. PCI/IB2018/059935, 2018. National Property Institute Intellectual —INAPI: Santiago, Chile.
- Michael, R.J., Courtwright, J.A., Ferro, E.B., Filiatrault, A., Higgins, P.S. and Wanitkorkul, A. (2010), "Development of a new base isolation system for seismic isolation of steel pallet storage racks", In *Proceedings of the 9th US National and 10th Canadian Conference on Earthquake Engineering (9USN10CEE)*, Toronto, ON, Canada (pp. 25-29).
- Miranda, E., Mosqueda, G., Retamales, R. and Pekcan, G. (2012), "Performance of nonstructural components during the 27 February 2010 Chile earthquake", *Earthq. Spectra*, **28**(1_suppl1), 453-471.
- Mucciarelli, M. and Liberatore, D. (2014), "Guest editorial: the Emilia 2012 earthquakes, Italy", *Bull. Earthq. Eng.*, **12**, 2111-2116.
- Pan, T.C. and Cui, W. (1998), "Response of segmental buildings to random seismic motions", *ISST J. Eng. Technol.*, **35**(4), 105-112.
- Pan, T.C., Ling, S.F. and Cui, W. (1995), "Seismic response of segmental buildings", *Earth. Eng. Struct. Dyn.*, **24**(7), 1039-1048.
- Pellegrino, J.B., Courtwright, J.A. and Michael, R. (2007), US Patent No. 7,263,806. Washington, DC: US Patent and Trademark Office.
- Perrone, D., Calvi, P.M., Nascimbene, R., Fischer, E.C. and Magliulo, G. (2019), "Seismic performance of non-structural elements during the 2016 Central Italy earthquake", *Bull. Earthq. Eng.*, **17**(10), 5655-5677.

- Rossi, L., Holtschoppen, B. and Butenweg, C. (2019), "Official data on the economic consequences of the 2012 Emilia-Romagna earthquake: a first analysis of database SFINGE", *Bull. Earthq. Eng.*, **17**, 4855-4884.
- Shaheen, M.S. and Rasmussen, K.J. (2022), "Development of friction-damped seismic fuses for steel storage racks", *J. Construct. Steel Res.*, **192**, 107216.
- Sideris, P., Filiatrault, A., Leclerc, M. and Tremblay, R. (2010), "Experimental investigation on the seismic behavior of palletized merchandise in steel storage racks", *Earthq. Spectra*, **26**(1), 209-233.
- Simoncelli, M., Tagliaferro, B. and Montuori, R. (2020), "Recent development on the seismic devices for steel storage structures", *Thin-Wall. Struct.*, **155**, 106827. <https://doi.org/10.1016/j.tws.2020.106827>.
- Tagliaferro, B., Rosario, M. and Maria Gabriella, C. (2021), "Shake table testing and numerical modeling of a steel pallet racking structure with a seismic isolation system", *Thin-Wall. Struct.*, **164**(2021), 107924.
- Tang, Z., Clifton, G., Lim, J., Maguire, J. and Teh, L. (2017), "Increasing seismic resilience of pallet racking systems using sliding friction baseplates", *In Proceedings of the 2017 New Zealand Society for Earthquake Engineering (NZSEE) Conference*, Wellington, New Zealand, 27-29.
- Uma, S.R. and Beattie, G. (2011), "Observed performance of industrial pallet rack storage systems in the canterbury earthquakes", *Bull. New Zealand Soc. Earthq. Eng.*, **44**(4), 388-393.
- Wang, S.J., Chang, K.C., Hwang, J.S., Hsiao, J.Y., Lee, B.H. and Hung, Y.C. (2012), "Dynamic behavior of a building structure tested with base and mid-story isolation systems", *Eng. Struct.*, **42**, 420-433.

CC

Nomenclature

- a : vertical distance between the upper damper support and its lower support (cm).
- b : horizontal distance between the upper damper support and the lower support (cm).
- b_a : inner width of the insulation platform (cm).
- b_t : external width of the isolation platform (cm).
- L_a : length of isolation platform (cm).
- L_t : length of isolation platform plus the safety distance (cm).
- d : diagonal distance between the upper damper support and the lower support (cm).
- F_I : inertial force (N).
- F_r : friction force (N).
- F_N : normal force (N).
- F_{Di} : dissipater force of i -th damper.
- F_{Ei} : elastic force of i -th spring.
- P : weight on the isolation system (N).
- v : displacement of the local degree of freedom (mm).
- \dot{v} : velocity of the local degree of freedom (cm/s).
- v_0 : precompression displacement of springs in the local degree of freedom (cm).
- u : displacement of the global degree of freedom (cm).
- \dot{u} : speed of the global degree of freedom (cm/s).
- \ddot{u} : relative acceleration with respect to the ground (cm/s²).
- θ : angle formed as a result of the vertical misalignment

between the upper and lower supports of the springs parallel to the shock absorbers.

m : total mass (platform + pallets) (kg).

g : gravitational acceleration (9.81 m/s²).

μ_{eq} : equivalent coefficient of friction.

$\bar{\mu}_{eq}$: average equivalent coefficient of friction.

\bar{E}_d : average energy dissipated per cycle (J).

$\bar{E}_d^{(Ex)}$: average dissipated energy per cycle obtained experimentally (J).

$\bar{E}_d^{(A.M.)}$: average dissipated energy per cycle obtained using the analytical model (J).

$k_s^{(A)}$: theoretical stiffness of springs (N/cm).

$k_s^{(E)}$: experimental stiffness of springs (N/cm).

T_I : isolation period (s).

d_w : wire diameter (mm).

D : mean diameter of the spring (mm).

G : shear modulus of steel (MPa).

N_a : number of active coils of springs.

N_c : number of charge-discharge cycles of the forcing.

ε_F : relative error between exp. and analytical spring stiffness.

F_v : force of the local degree of freedom of the damper.

F_u : force of the overall degree of freedom of the damper.

β : angle formed due to the vertical misalignment between the upper and lower supports of the shock absorbers.

$\bar{F}_{t,c}^{max}$: maximum compression and traction force of the shock absorbers.

f_{ai} : auxiliary function used for the analytical model.

ε_{E_d} : relative error between experimental and analytical dissipated energy.

ε_F : relative error between experimental and analytical force.

\ddot{u}_g : Ground acceleration (input).

$u_{g,max}^{(abs.)}$: maximum absolute ground displacement

$\ddot{u}_{g,max}^{(abs.)}$: maximum absolute ground acceleration

$u_{max}^{(rel.)}$: maximum relative pallet-rack displacement

$\ddot{u}_{max}^{(abs.)}$: maximum absolute pallet-rack acceleration

$Q_{0,max}^{(I.S.)}$ (m): max. shear load of pallet with mass m isolated.

$Q_{0,max}^{(fixed)}$ ($full$): max. pallet-rack shear load with full loading mass fixed to the rack.